We are IntechOpen, the world's leading publisher of Open Access books Built by scientists, for scientists

6,900
Open access books available

185,000
International authors and editors

200M
Downloads

Our authors are among the

154
Countries delivered to

TOP 1%
most cited scientists

12.2%
Contributors from top 500 universities



WEB OF SCIENCE™

Selection of our books indexed in the Book Citation Index in Web of Science™ Core Collection (BKCI)

Interested in publishing with us?
Contact book.department@intechopen.com

Numbers displayed above are based on latest data collected.
For more information visit www.intechopen.com



Chapter 8

Typical Non–TiO_2-Based Visible-Light Photocatalysts

Pengyu Dong, Xinguo Xi and Guihua Hou

Additional information is available at the end of the chapter

http://dx.doi.org/10.5772/62889

Abstract

Photocatalysis has received much attention as a potential solution to the worldwide energy shortage and for counteracting environmental degradation. However, the traditional photocatalyst, TiO_2, cannot make use of visible light that accounts for 45% of solar spectrum because of a large bandgap (3.2 eV). Therefore, it is urgent to develop visible-light-driven photocatalysts. On the one hand, some modification technologies were explored to extend the light absorption of TiO_2 to visible-light region, such as doping of metal and non-metal elements, dye sensitization, and so on. On the other hand, much effort has been directed toward the development of new visible-light photocatalysts. The good news is, some novel and efficient non-TiO_2-based photocatalysts have been discovered, such as WO_3, Ag_3PO_4, $BiVO_4$, g-C_3N_4. In this chapter, these four typical visible light–driven semiconductor photocatalysts were highlighted. WO_3 is a visible light–responsive photocatalyst that absorbs light up to ca. 480 nm. Besides that, WO_3 has some advantages, such as low cost, harmlessness, and stability in acidic and oxidative conditions. Preparation of WO_3 films with the deposition of noble metal is considered to be a promising approach for the photocatalytic applications. In addition, the characteristic morphology and improved photocatalytic performance of Ag_3PO_4-based and $BiVO_4$-based have been raised up. New methods for fabrication Ag_3PO_4 with exposed high-energy facets and novel heterogeneous Ag_3PO_4 co-catalysts have been developed. Monoclinic $BiVO_4$ is a promising photo-anode material for photocatalytic water splitting to produce hydrogen. Co-catalysts loaded on $BiVO_4$ could improve the surface charge transfer efficiency. Furthermore, g-C_3N_4 is a promising visible-light photocatalyst due to its unique electronic structure. To date, g-C_3N_4-based photocatalysis has become a very hot research topic. The synthesis, bandgap engineering, and semiconductor composites of g-C_3N_4-based photocatalysts are highlighted.

Keywords: visible-light-driven photocatalysts, WO_3, Ag_3PO_4, $BiVO_4$, g-C_3N_4, structures, morphologies, heterojunction

INTECH
open science | open minds

© 2016 The Author(s). Licensee InTech. This chapter is distributed under the terms of the Creative Commons Attribution License (http://creativecommons.org/licenses/by/3.0), which permits unrestricted use, distribution, and reproduction in any medium, provided the original work is properly cited. CC BY

1. Introduction

In the past decades, the development of photocatalysis has been the focus of considerable attention with photocatalysis being used in a variety of products across a broad range of research areas, including especially environmental and energy-related fields [1]. The pioneering discovery from the water splitting reported by Fujishima and Honda in 1972 [2] is considered to be unlock the doors of the photocatalysis research. This is because they found that the photocatalytic properties of certain materials could convert solar energy into chemical energy to oxidize or reduce materials to obtain useful materials including hydrogen [3, 4] and hydrocarbons [5] and to remove pollutants and bacteria [6] on wall surfaces and in air and water [7]. Among the various photocatalysts developed, TiO_2 is undoubtedly the most popular and widely used photocatalyst since it is of low cost, high photocatalytic activity, chemical, and photochemical stability [8]. However, due to the wide bandgap of TiO_2, it could absorb and utilize ultraviolet (UV) light, which accounts for a small fraction of solar light (3–5%). Hence, it is necessary to develop a particular photocatalyst, which is sensitive to sunlight. The range of optical absorption of TiO_2 could be extended from UV to visible light, which is a good way to utilize of solar energy effectively in photocatalytic reactions. In the past decades, researchers spent a great deal of time and resources developing visible light–active photocatalysts [9]. In order to design visible-light response photocatalysts, two strategies have been proposed. One approach is the modification of the wide bandgap photocatalysts (such as TiO_2, ZnO) by doping or by producing between them and other materials. The other approach is the exploration and development of novel semiconductor materials capable of absorbing visible light.

From the view point of using solar light, the first step in the development of a technology that makes efficient use of solar energy is the discovery of a photocatalyst that becomes highly active under visible light ($\lambda > 400$ nm). Since the optical absorption properties of a photocatalyst is determined by the energy bandgap of semiconductor photocatalyst, it is necessary to choose a narrow band of semiconductor as photocatalyst. Hence, the energy band engineering is a fundamental aspect of the design and fabrication of visible-light–driven photocatalysts. Considering the optical absorption, direct, and narrow bandgap semiconductors are more likely to exhibit high absorbance and be suitable for the efficient harvesting of low-energy photons. However, it is a pity that the recombination probability for photo-excited electron–hole pairs is rather high in direct and narrow bandgap semiconductors, and the band-edge positions are frequently incompatible with the electrochemical potential that is necessary to trigger specific redox reactions [10]. Therefore, the energy band structure of a photocatalyst plays a significant role in the light absorption property and in determining the redox potentials. In order to effectively utilize the solar energy, design and adjustment of band structure are an effective approach to obtain visible-light response photocatalyst with excellent performance. Through unremitting efforts, researchers have developed some typical and excellent visible-light-driven semiconductor photocatalysts, such as WO_3, Ag_3PO_4, $BiVO_4$, g-C_3N_4-based photocatalysts, which possess suitable energy band configurations. In this chapter, we would like to focus on these four typical visible-light-driven semiconductor photocatalysts and summarize the recent progress of enhanced visible-light efficiency.

Furthermore, we also highlight the crucial issues that should be addressed in future research activities.

2. WO_3-based photocatalysts

2.1. Structures and morphologies of WO_3

The crystal structures of WO_3 are described below: WO_3 crystals are generally formed by corner and edge sharing of WO_6 octahedra. The following phases are obtained by corner sharing: monoclinic II (ε-WO_3), triclinic (δ-WO_3), monoclinic I (γ-WO_3), orthorhombic (β-WO_3), tetragonal (α-WO_3), and cubic WO_3 [11]. However, cubic WO_3 is not commonly observed experimentally. Szilágyi et al. [12] found that the monoclinic WO_3 always shows the best photocatalytic activity among these crystal phases.

The electronic band structure of WO_3 can be described as follows: WO_3 is an n-type semiconductor, with an electronic bandgap (Eg), corresponding to the difference between the energy levels of the valence band (VB), formed by filled O 2p orbitals and the conduction band (CB) formed by empty W 5d orbitals [13]. It is known that the cubic phase is the ideal crystal phase of WO_3, and the crystal phase changes with the distortion degree from the ideal phase, which is accompanied by a change in Eg since the occupied levels of the W 5d states change [14]. As a photocatalytic material, stoichiometric WO_3 has a CB edge, which is positioned slightly more positive (versus NHE (normal hydrogen electrode)) than the H_2/H_2O reduction potential [15] and a VB edge much more positive than the H_2O/O_2 oxidation potential, which makes WO_3 capable of efficiently photo-oxidizing a wide range of organic compounds [16] such as textile dyes and bacterial pollutants. When compared to TiO_2, another advantage of WO_3 is that it can be irradiated by the blue region of the visible solar spectrum. Furthermore, WO_3 has a remarkable stability in acidic environments, making it a promising candidate for treatment of water contaminated by organic acids [17].

The preparation of nanometer-sized crystalline WO_3 particles and control of their morphology is important to improve photocatalytic activity. Zhao and Miyauchi [18] developed a facile and economical method to produce high-purity tungstic acid hydrate nanotubes and nanoporous-walled WO_3 nanotubes on a large scale. They found that the WO_3 nanotubes loaded with Pt nanoparticles show larger surface area and higher visible-light-driven photocatalytic activity compared to Pt-nanoparticle-loaded commercial WO_3. Recently, attention has been focused on three-dimensionally ordered macroporous (3DOM) materials with pores sizes in the sub-micrometer range, because of the potential of photocatalysis application. Generally, the 3DOM materials can be prepared by three steps. Firstly, some mono-disperse polymer spheres such as poly(methyl methacrylate) (PMMA), and polystyrene (PS) were selected as a colloidal crystal template. Secondly, the colloidal crystal template was immersed into the material precursors. Thirdly, the polymer colloidal crystal template was removed by the calcination removed to form an ordered porous structure. The ordered ("inverse opal") structures prepared by this method consist of a skeleton surrounding and a uniform close-

packed macropores. For instance, Sadakane et al. [19] prepared 3DOM WO_3 using a colloidal crystal template of PMMA spheres.

2.2. WO_3 films and photocatalytic applications

Generally, WO_3 exhibits low photocatalytic activity for decomposing organic compounds compared with traditional TiO_2 photocatalyst under UV light irradiation. However, WO_3 could show high photocatalytic activity for the decomposition of organic compounds under visible light when the surface is modified with noble metal nanoparticles, such as platinum (Pt), palladium (Pd), and so on. For instance, Abe et al. demonstrated that WO_3 deposited with Pt nanoparticles exhibits good photocatalytic activity for the decomposition of liquid and gaseous organics. It was an impressive performance that the photocatalytic activity of Pt/WO_3 was almost close to that of TiO_2 under UV light irradiation and much higher than that of N-doped TiO_2 under visible irradiation [20]. In the Pt/WO_3 system, the electrons were excited to the CB from the VB of WO_3 and then were injected into Pt nanoparticles, which act as electron pools to participate in two or four electron reductions of the adsorbed oxygen molecules. Hence, the particle size of the Pt nanoparticles plays a very important role in the multi-electron reduction process. On the other side, the metal surface of Pt induces the photocatalyst is more hydrophobic compared with a metal oxide surface. These findings were widely concerned in the past years and were considered to open up a research upsurge of WO_3 photocatalyst.

Large area uniformity, low production cost, and excellent durability of WO_3 thin films can play a very important role in the fabrication of electrochromic devices and photocatalytic materials. In the past years, the electrodeposition, sol–gel processing, one-pot direct hydrothermal growth, chemical vapor deposition, sputtering, and vacuum evaporation methods were used to prepare WO_3 thin films. In particular, Miyauchi M synthesized WO_3 films with underlying Pt nanoparticles (WO_3/Pt/substrate) and those with overlying Pt nanoparticles (Pt/WO_3/substrate) by sputtering and sol–gel methods [21]. **Figure 1** shows the SEM images of different Pt layer surfaces. Moreover, it is found that underlying Pt nanoparticles greatly enhanced the photocatalytic oxidation activity of WO_3 without decreasing the photo-induced hydrophilic conversion between these films. The optimum structure for high performance in both photocatalysis and photo-induced hydrophilicity was WO_3 (50 nm)/Pt(1.5 nm)/substrate, and this film exhibited a significant self-cleaning property even under visible-light irradiation.

3. Ag_3PO_4-based photocatalysts

In 2010, a breakthrough on visible-light-driven photocatalysts was made by Ye's research team, who reported the use of Ag_3PO_4 as an active visible-light-driven photocatalyst for the oxidation of water and photodecomposition of organic compounds [22]. Ye's research team demonstrated that Ag_3PO_4 photocatalyst could achieve high quantum efficiency under visible-light irradiation. The quantum efficiency of this novel photocatalyst could up to 90% which is significantly superior to others such as $BiVO_4$ or N-doped TiO_2. However, it should be noted that there are still some limitations in the Ag_3PO_4 photocatalytic system. Firstly, the particle

http://dx.doi.org/10.5772/62889

size of Ag_3PO_4 is relatively large (0.5–2 μm) that limits the photocatalytic performance. To enhance photocatalytic activity of this new material, it is desirable to synthesize nanosized Ag_3PO_4 particles with higher surface area which is beneficial to the photocatalytic reaction. Secondly, the Ag_3PO_4 photocatalyst suffers from serious stability issue which is the main hindrance for the practical application of Ag_3PO_4 as a recyclable and highly efficient photocatalyst. This is because the CB potential of Ag_3PO_4 is more positive than that of the hydrogen potential (0 V). As shown in **Figure 2**, the CB and VB potentials of Ag_3PO_4 are +0.45, +2.9 V vs. NHE, respectively [23]. Thus, under visible-light irradiation, electrons and holes were generated in the CB and VB of Ag_3PO_4, and then, the photogenerated electrons could reduce

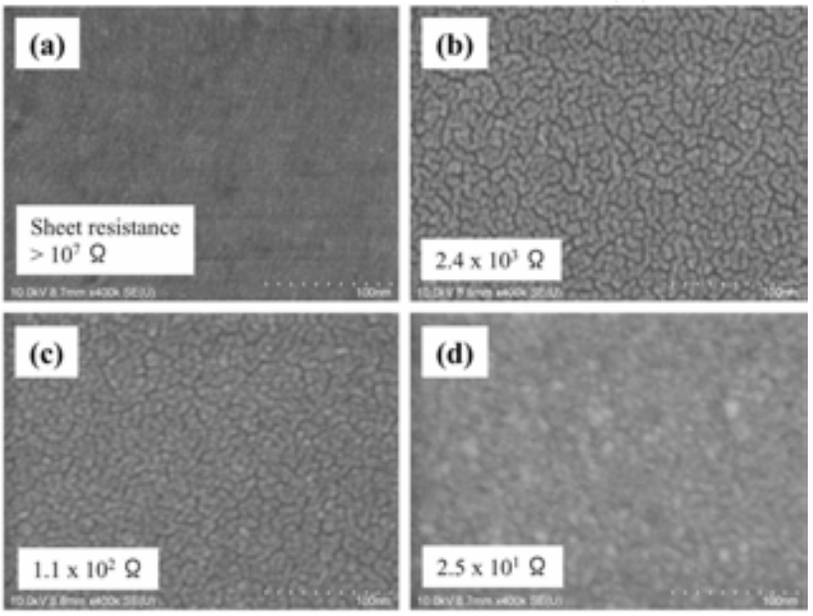


Figure 1. SEM images of different Pt layer surfaces: (a) 0.5 nm, (b) 1.5 nm, (c) 3 nm, and (d) 10 nm thick. The inset words describe the sheet resistance of the film surfaces measured by a four-pin probe method (reproduced with permission from [21]).

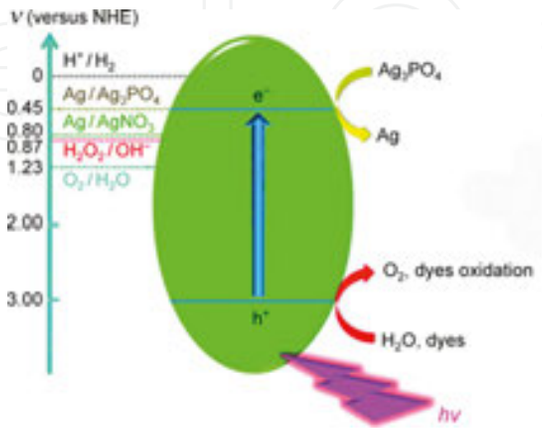


Figure 2. Schematic drawing of redox potentials of Ag_3PO_4 (reproduced with permission from [23]).

the interstitial silver ions (Ag^+) to form the silver atoms (Ag), resulting in the photocorrosion of Ag_3PO_4 without a sacrificial reagent. The formed Ag nanoparticles would adhere to the surface of the Ag_3PO_4 photocatalyst and suspend in the photocatalytic reaction systems, giving rise to the prevention of absorption of visible light and the decrease of photocatalytic activity [24]. Hence, it is necessary to enhance the photocatalytic activity and stability of Ag_3PO_4.

3.1. Morphology-controlled syntheses of Ag_3PO_4

The morphology control of photocatalysts has been considered to be one of the most promising avenues to improve the photocatalytic properties. This is because photocatalytic reactions are typically surface-based processes, and thus, the photocatalytic efficiency is closely related to the morphology and microstructure of a photocatalyst. Accordingly, further studies on Ag_3PO_4 crystals with new morphologies and structures will be of great value.

To investigate the effects of the shapes and facets of particular photocatalysts on their photocatalytic properties, single-crystals of Ag_3PO_4 were synthesized in two forms by Ye's research team [25], firstly with rhombic dodecahedron shapes and exposed {110} facets, and secondly cubes bounded by {100} facets. Ye's research team found that rhombic dodecahedral Ag_3PO_4 crystals could be prepared using CH_3COOAg as the silver ion precursors, while cubic Ag_3PO_4 crystals could be prepared using $[Ag(NH_3)_2]^+$ as the silver ion precursors. The Ag_3PO_4 dodecahedrons were formed by 12 well-defined {110} planes with cubic crystal symmetry (**Figure 3a**), whereas the Ag_3PO_4 cubes showed sharp corners, edges, and smooth

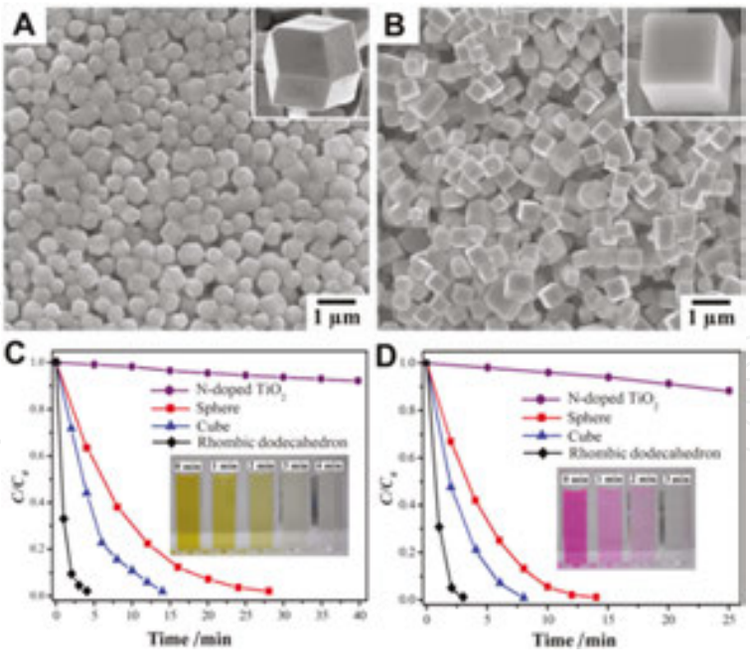


Figure 3. SEM images of Ag_3PO_4 sub-microcrystals with different morphologies: (A) rhombic dodecahedrons and (B) cubes. The photocatalytic activities of Ag_3PO_4 rhombic dodecahedrons, cubes, spheres, and N-doped TiO_2 are shown for the degradation of (C) MO and (D) RhB under visible-light irradiation ($\lambda > 400$ nm) (reproduced with permission from [25]).

http://dx.doi.org/10.5772/62889

surfaces (**Figure 3b**). The results of photocatalytic degradation of methyl orange (MO) and RhB dyes indicated that the rhombic dodecahedral Ag_3PO_4 exposed {110} facet showed higher photocatalytic activity than the cubic Ag_3PO_4 exposed {100} facet (**Figure 3c**, **d**) under visible-light irradiation, which is in accordance with the higher surface energy of 1.31 J/m^2 for the {110} facet compared to 1.12 J/m^2 for the {100} facet.

Very recently, some morphologies of Ag_3PO_4 have been reported by other research teams. For examples, Liu and co-workers [26] reported Ag_3PO_4 crystals with porous structure. Guo and co-workers synthesized tetrahedral Ag_3PO_4 crystals with exposed {111} facets and tetrapod-shaped Ag_3PO_4 microcrystals with exposed {110} facets [23, 27]. Teng and co-workers [28] synthesized Ag_3PO_4 crystals with tetrapod morphology by a hydrothermal method. Liang et al. [29] synthesized hierarchical Ag_3PO_4 porous microcubes with enhanced photocatalytic properties. However, these reported various morphologies of Ag_3PO_4 crystals were obtained by adjusting internal experimental conditions such as raw materials, solvents, pH values, and additives. Our research team found that the Ag_3PO_4 products with various new morphologies such as branch, tetrapod, nanorod, and triangular prism were prepared via a facile and efficient synthesis process [30], as shown in **Figure 4**. It is demonstrated that the morphology of Ag_3PO_4 crystals can be controlled by simply adjusting external experimental conditions such as static and ultrasonic conditions. When the product was prepared under static conditions for 0 h, branched Ag_3PO_4 was achieved. Increasing the static time led to the formation of

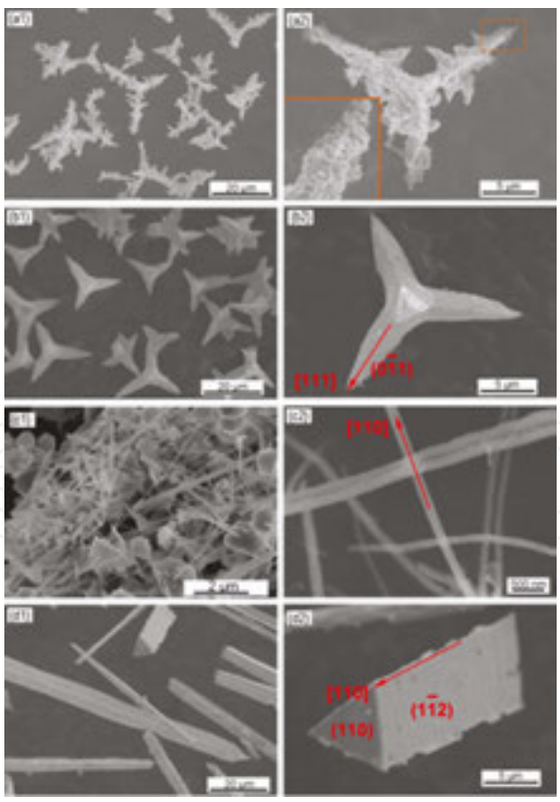


Figure 4. SEM images of branched (a), tetrapod (b), nanorod-shaped (c), and triangular-prism-shaped (d) Ag_3PO_4 crystals (reproduced with permission from [30]).

tetrapod morphology. When the synthesis process was completed under ultrasonic conditions within 2 h, nanorod-shaped Ag_3PO_4 was obtained. Prolonging the ultrasonic time could result in the formation of triangular-prism-shaped Ag_3PO_4. The photocatalytic results indicate that the branched Ag_3PO_4 sample shows greatly enhanced photocatalytic activity compared with other as-prepared Ag_3PO_4 samples.

3.2. Theoretical study of the electronic structure of Ag_3PO_4

To elucidate its mechanism of the extremely high photo-oxidative activity under visible-light irradiation of Ag_3PO_4, theoretical works have been carried out using first-principle method. So far, theoretical investigations are mainly focused on the energy band configuration because photo-excited carriers are generated when the incident photon energy is higher than the bandgap of Ag_3PO_4. Besides that, the alignment between the band edges and the redox potentials of the target molecules should also be considered. This is because the photogenerated electrons can be transferred to the adsorbed oxygen molecules only when there is a sufficiently large negative offset of the conduction band minimum (CBM), and the photogenerated holes could combine with water molecules when there is a sufficiently large positive offset of the valence band maximum (VBM) according to the redox potentials [31].

To obtain insight into the high photo-oxidative activity of Ag_3PO_4, *ab initio* density functional theory (DFT) calculations have also been carried out by Ye's research team [22]. It is found that Ag_3PO_4 is an indirect bandgap semiconductor, and the bottoms of the CB are mainly composed of hybridized Ag 5s5p as well as a small quantity of P 3s orbitals, whereas the tops of the VB are composed of hybridized Ag 4d and O2p orbitals. Moreover, Ye's research team further studied the electronic structures of three different Ag-based oxides Ag_3PO_4, Ag_2O, and $AgNbO_3$ to understand the high photocatalytic performance of Ag_3PO_4 [32]. The total and local DOS results were shown in **Figure 5**. The calculated DOS results revealed that the CBM of Ag_3PO_4 is made up of Ag s states due to the formation of the rigid tetrahedral units PO_4, which decrease and increase the strength of Ag–O and Ag–Ag bonds, respectively. This induces to a very dispersive electronic structure at the CBM, resulting in a highly delocalized and isotropic distribution of wave function. Therefore, they conclude that the excellent photocatalytic performance of Ag_3PO_4 is attributed partly to the highly dispersive band structure of the CBM, resulting from Ag s–Ag s hybridization without localized d states.

In addition, Ma et al. [33] used first-principles density functional theory incorporating the LDA + U formalism to investigate the origin of photocatalytic activation of Ag_3PO_4. They found that Ag_3PO_4 has a great distribution of CB and the inductive effect of PO_4^{3-}, which is benefit for the separation of photogenerated electron–hole pairs. It is theoretically demonstrated that Ag vacancies in Ag_3PO_4 with high concentration have an evident influence on the separation of electron–hole pairs and the optical absorbance of visible light, which presents a rational interpretation of the experimental results of high photocatalytic activity of Ag_3PO_4.

http://dx.doi.org/10.5772/62889

3.3. Ag_3PO_4-based composites

To harvest photons in visible region, many narrow bandgap metal oxides or chalcogenides have been coupled with TiO_2 to fabricate visible-light photocatalysts, which exhibit visible-light photocatalytic activity to a certain extent. Such a strategy is also applied to modify Ag_3PO_4 photocatalyst to enhance its photocatalytic activity and/or improve its stability.

Recent reports indicated that the insoluble AgX (X = Cl, Br, I) nanoshells on the surface of Ag_3PO_4 could improve its photocatalytic activity and stability [24]. In addition, various coupled systems, such as Ag_3PO_4/TiO_2 [34], Ag_3PO_4/Ag [35] composites have been developed to improve the photocatalytic activity and/or stability of Ag_3PO_4. Our research team found that Ag_3PO_4 and reduced graphite oxide sheets (RGOs) nanocomposites show the enhanced photocatalytic activity and structural stability [36]. We also found that, when Ag_3PO_4 and $TiOF_2$ were compounded, the stability of composite photocatalysts was highly enhanced but the photocatalytic activity was not improved. In the case of $Ag_3PO_4/TiOF_2$ composite, Ag_3PO_4 and $TiOF_2$ have different conduction bands (Ec), valence bands (Ev), and Fermi levels (Ef) (the detail analysis of level energies was shown in the Supplementary data). When the mixed $Ag_3PO_4/TiOF_2$ composite is formed, the Fermi energies of these two phases have to be the same in the boundary between the Ag_3PO_4 and $TiOF_2$ phases. This leads to both of the Ec and Ev of Ag_3PO_4 lie above that of $TiOF_2$, as shown in **Figure 6**. Under visible-light irradiation, a larger number of electrons are excited to the Ec from the Ev of Ag_3PO_4 and then transferred to the Ec of $TiOF_2$, while the holes left on the VB of Ag_3PO_4. Thus, the enriched electrons on the surface of $TiOF_2$ could facilitate their participation in a multiple-electron reduction reaction of oxygen ($O_2 + 2H^+ + 2e^- \rightarrow H_2O_2$), which effectively protects Ag_3PO_4 semiconductors to avoid its self-corrosion by a single-electron reduction reaction ($Ag^+ + e^- \rightarrow Ag$). Therefore, the Ag_3PO_4/

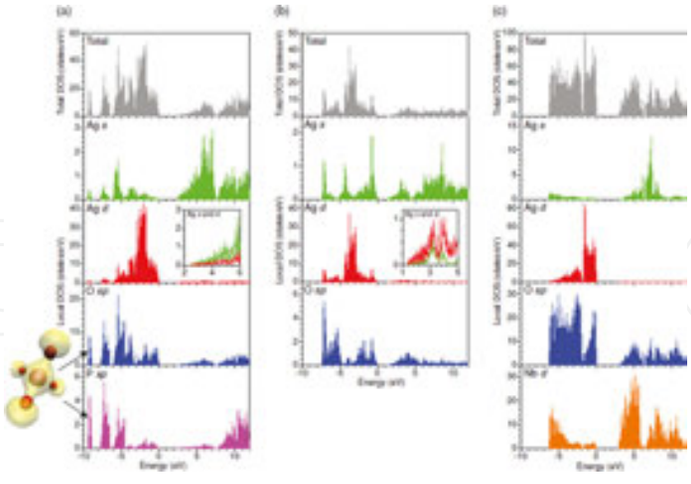


Figure 5. (Color) Total and local DOS for (a) Ag_3PO_4, (b) Ag_2O, and (c) $AgNbO_3$. For the local DOS, we use spheres of radii 1.503, 0.82, 1.233, and 1.503 Å for Ag, O, P, and Nb, respectively. The VBM represents the zero energy. The insets in (a) and (b) display the extended plots of DOS for Ag s and d at the energy range near the CBM. The partial charge density corresponding to one of the P-O bonding states is illustrated in the leftmost area in (a). The mauve and red spheres denote the positions of P and O atoms, and the isosurface (yellow surface) is at 0.03 e/Å^3, respectively (reproduced with permission from [32]).

$TiOF_2$ composite photocatalyst exhibits enhanced photocatalytic stability compared with that of pure Ag_3PO_4. It is thought that $TiOF_2$ was used as an electron acceptor and protected Ag_3PO_4 particles to avoid the self-corrosion of Ag_3PO_4. On the other hand, the left holes on the VB of Ag_3PO_4 could migrate to the surface of photocatalysts and participate in the photo-oxidative reaction and then decompose the methylene blue (MB) molecules.

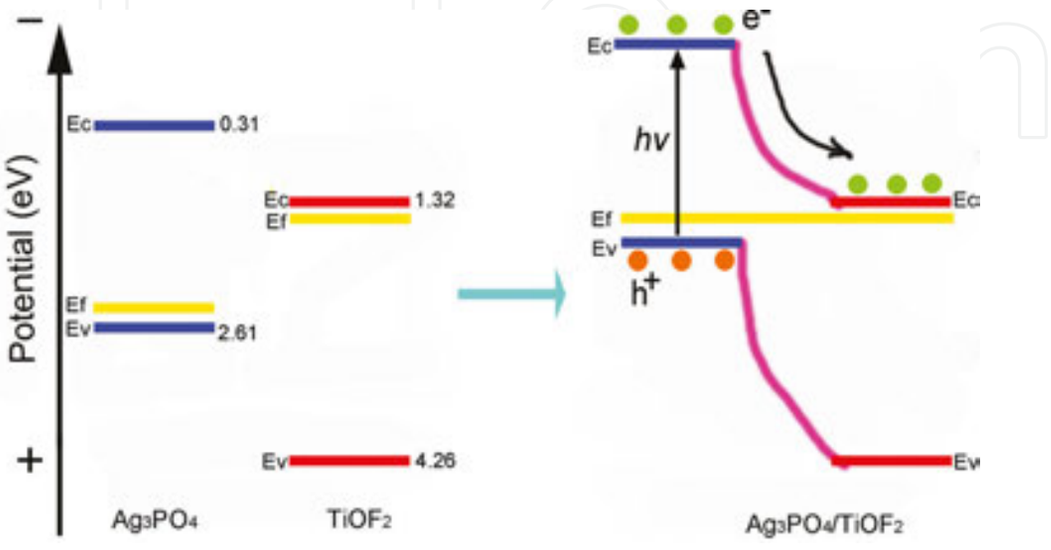


Figure 6. Schematic diagram for the CB, VB, and Fermi level of Ag_3PO_4 as well as $TiOF_2$, and the electron–hole separation and energy band matching of $Ag_3PO_4/TiOF_2$ composite under visible-light irradiation (reproduced with permission from [37]).

4. $BiVO_4$-based photocatalysts

$BiVO_4$ is one of the typical complex oxides with narrow bandgap, which possess excellent visible-light photocatalytic properties. As an n-type semiconductor with a direct bandgap of 2.4 eV, $BiVO_4$ could absorb ample visible light and is stable in neutral electrolyte, nontoxic, and relatively cheap [38]. $BiVO_4$ has three crystal systems of zircon-tetragonal, scheelite tetragonal, and scheelite-monoclinic. However, only the scheelite-monoclinic phase is reportedly active in the photocatalytic oxygen evolution [39]. In addition, the scheelite-monoclinic can be obtained from the irreversible phase transformation of the zircon-tetragonal structure at the temperature of 400–500°C [40].

4.1. Syntheses of $BiVO_4$ with different morphologies

$BiVO_4$ could be synthesized by various methods, such as solid-state reaction, metal organic decomposition, hydrothermal treatment, and coprecipitation.

$BiVO_4$ prepared via a solid-state reaction always shows big particle size and low surface area, which resulted in poor photocatalytic activity. So, it is encouraged to synthesize $BiVO_4$ by new methods.

http://dx.doi.org/10.5772/62889

Zhang et al. [41] reported $BiVO_4$ nanosheets were hydrothermally synthesized by a simple one-step route in the presence of sodium dodecyl benzene sulfonate (SDBS) as a morphology-directing template. The $BiVO_4$ nanosheets had a monoclinic structure, were ca. 10–40 nm thick, and showed a preferred (010) surface orientation.

Single-crystalline $BiVO_4$ microtubes with square cross sections and flower-like morphology was prepared by a facile reflux method at 80°C [42]. In the synthesis process, no surfactants or templates were involved. The prepared microtubes show the monoclinic structure with a growth direction of [010], and the side length is about 800 nm as well as the wall thickness is around 100 nm.

Li et al. [43] describes a nanocasting synthesis of ordered mesoporous $BiVO_4$ photocatalyst with the help of a template of silica (KIT-6) using ammonia metavanadate and bismuth nitrate hydrate as vanadium and bismuth sources, respectively. Monoclinic scheelite $BiVO_4$ crystals were formed inside the mesopores of hard template (silica) by a mild thermal process, and mesoporous $BiVO_4$ was obtained after the removal of silica by NaOH treatment. The prepared mesoporous $BiVO_4$ showed not only the activity for photocatalytic O_2 evolution but also the photocatalytic oxidation of NO gas in air under visible-light irradiation.

In particular, Li's research team prepared $BiVO_4$ crystals exposed with {010} and {110} crystal facets, as shown in **Figure 7**. They found that the reduction reaction with photogenerated electrons occurs separately on the {010} facet under visible-light irradiation, while the oxidation reaction with photogenerated holes takes place on the {110} facet. Therefore, a conclusion that efficient charge separation can be achieved on different crystal facets was given. Based on this finding, they further demonstrated that the reduction and oxidation co-catalysts could be selectively deposited on the {010} and {110} facets, respectively, giving rise to a much higher photocatalytic and photo-electrocatalytic activity for water oxidation reactions than the photocatalyst with randomly distributed co-catalysts. Overall, these results indicate that the photogenerated electrons and holes can be separated between the different facets of semiconductors.

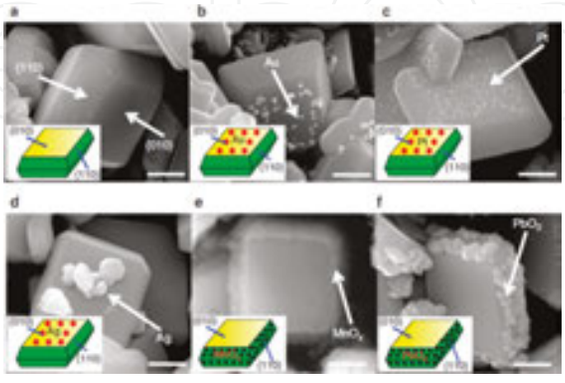


Figure 7. SEM images of $BiVO_4$ (a), $Au/BiVO_4$ (b), $Pt/BiVO_4$ (c), $Ag/BiVO_4$ (d), $MnOx/BiVO_4$ (e), and $PbO_2/BiVO_4$ (f). The deposited contents of the metals/metal oxides are all 5 wt%. The scale bar is all 500 nm (reproduced with permission from [44]).

4.2. Modification of $BiVO_4$ with enhanced photocatalytic performance

Heterostructure formation is widely utilized to improve the properties of a semiconductor by combining with other functional materials. It has a large scope of materials as well as applications including photocatalysis, photovoltaics, light-emitting devices, and optoelectronics [45]. Combination of two semiconductors (n/n or p/n) with proper band positions can make cascade electron transfer from CB of upper potential to CB of lower potential. Successful heterojunction formation of $BiVO_4$ has been reported with WO_3, SnO_2, Fe_2O_3, $CuWO_4$, and CdS, in which the $WO_3/BiVO_4$ has been the most common. WO_3 (Eg = 2.6–2.8 eV) is one of the most active metal oxide photocatalyst with CB at 0.42 V_{RHE} (RHE: reversible hydrogen electrode) and VB at 3.12 V_{RHE} [46]. With such band configurations presented at **Figure 8a**, the photo-induced electrons transfer from $BiVO_4$ to WO_3, whereas holes cannot. This prevents electron/hole recombination in $BiVO_4$. Since WO_3 has better mobility and longer diffusion length than $BiVO_4$, the photo-induced electrons collected in WO_3 can be more efficiently converted to photocurrents with much reduced recombination compared to the case when the photo-induced electrons are locked in $BiVO_4$. Since $BiVO_4$ has a smaller bandgap and wider pH stability, $BiVO_4/WO_3$ heterojunction can absorb larger portion of solar light and has better neutral stability compared with pure WO_3. The improved charge transfer characteristics of $BiVO_4/WO_3$ heterojunction was confirmed by electrochemical impedance spectroscopy (EIS) that showed that resistance of the heterojunction is reduced almost to that of WO_3. Moreover, nanostructured WO_3 was found to be more effective. As shown in **Figure 8b**, WO_3 prepared in one-dimensional (1D) nanorods or nanowires makes the $BiVO_4/WO_3$ heterojunction more effective [47]. The particular geometry reduces the distance that the photo-induced holes have to travel in radial direction to reach the surface of WO_3 photocatalyst. On the other hand, the photo-induced electrons have to flow along the axial direction making a vectorial flow. Another successful heterojunction is $BiVO_4/SnO_2$, as shown in **Figure 8c**. SnO_2 has a large bandgap of 3.5 eV and potentials of CB (0.27 V_{RHE}) and VB (3.77 V_{RHE}), which are favorable for cascade the photo-induced electron transferred from $BiVO_4$ [48]. In addition, SnO_2 has a passivation effect of FTO glass. Thus, a large number of interfacial defects and the potential

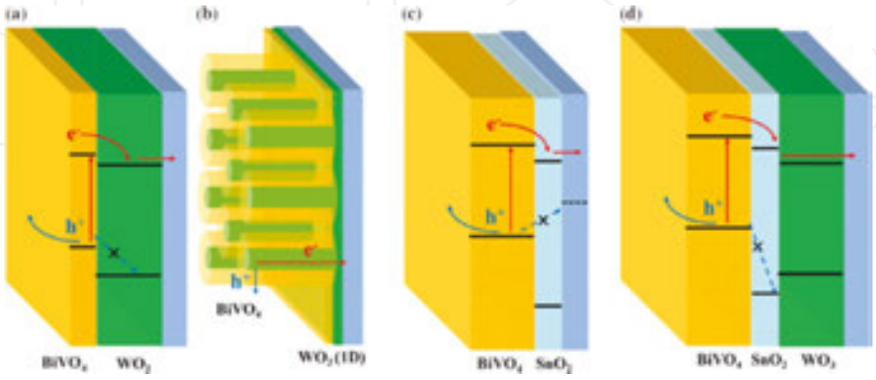


Figure 8. Schemes of $BiVO_4$-based heterojunction: (a) $BiVO_4/WO_3$ [46], (b) $BiVO_4/WO_3$ 1D nanostructure [47], (c) $BiVO_4/SnO_2$ (hole mirror) [49, 50], and (d) $BiVO_4/SnO_2/WO_3$ dual-hole mirror [48] (reproduced with permission from [46–50]).

electron trap states of FTO can be passivated by a thin SnO_2 layer, improving charge transfer at $BiVO_4$/FTO interface [49]. Also very positive VB of SnO_2 prevents a backward hole transfer through SnO_2 layer forming a "hole mirror." As CB potential of $BiVO_4$, SnO_2, and WO_3 is aligned in cascade (0.02/0.27/0.41 V_{RHE}), ternary composite of $BiVO_4/SnO_2/WO_3$ could be prepared as an effective heterojunction, as shown in **Figure 8d** [48].

5. g-C_3N_4-based photocatalysts

Since the pioneering work in 2009 on graphitic carbon nitride (g-C_3N_4) for visible-light photocatalytic water splitting [51], g-C_3N_4-based photocatalysis has become a very hot research topic. Unlike TiO_2, which is only active in the UV region, g-C_3N_4 has a bandgap of ca. 2.7 eV, with the CB and VB positions at ca. −1.1 and ca. +1.6 eV vs. NHE, respectively. This electronic structural character suggests the g-C_3N_4 could be a visible-light active photocatalyst. g-C_3N_4 is not only the most stable allotrope of carbon nitrides at ambient atmosphere, but it also has rich surface properties that are attractive for catalysis application due to the presence of basic surface sites. The ideal g-C_3N_4 consists solely of an assembly of C–N bonds without electron localization in the π state (this material is a π-conjugated polymer).

5.1. Syntheses of pristine g-C_3N_4

The most common precursors used for chemical synthesis of g-C_3N_4 are reactive nitrogen-rich and oxygen-free compounds containing prebonded C–N core structures, such as triazine and heptazine derivatives, but most of them is unstable and difficult to obtain and/or highly explosive. The synthesis of single-phase sp^3-hybridized carbon nitrides is a challenging task due to their low thermodynamic stability. Generally, the defect materials are much more valuable than the ideal one, in particular for catalysis, which requires surface defects. Thus, the synthesis of g-C_3N_4 with defects is an interesting topic, when the material is going to be used in catalysis.

Pure g-C_3N_4 can be obtained at ca. 500°C when the precursor cyanamide is pretreated with a basic solution (like aqueous NaOH) [52]. It is found that the presence of hydroxyl ions facilitates the transformation of cyanamide to g-C_3N_4, probably due to the hydroxyl ions that promote the condensation process, by reacting with the hydrogen atoms on the edges of the intermediate.

Generally, porous photocatalysts are very fascinating, because the porous structure can provide a large surface area and a lot of channels, which is benefit for the diffusion of contaminant molecules, as well as charge migration and separation. Researchers always synthesize the porous g-C_3N_4 photocatalyst using hard and soft templates because the porous structure of g-C_3N_4 can be tuned by choosing different templates. Recently, porous g-C_3N_4 can also be synthesized using surfactants (e.g., Triton X-100, P123, Brij 58) or ionic liquids as soft templates through a self-polymerization reaction [53].

1D nanostructured photocatalysts such as nanorods, nanowires, nanobelts, and nanotubes continue to attract special attention. This is because unique chemical, optical, and electronic

properties can be achieved by tuning their length, diameter, and aspect ratio, which is beneficial for optimizing their photocatalytic activity. For example, g-C_3N_4 nanorod networks were fabricated by a solvothermal method using cyanuric chloride and melamine in a sub-critical acetonitrile solvent [54]. It needs only a temperature of 180°C, which is much lower than that of traditional solid-state synthesis method (normally 500–600°C). The as-prepared sample mainly consists of regularly nanorods (accounts for 90%). The average diameter of these nanorods is 50–60 nm, and the length is about several micrometers.

5.2. Bandgap engineering of g-C_3N_4

Bandgap engineering of g-C_3N_4 to control its light-absorption ability and redox potential plays an important role in enhancing its photocatalytic performance. The main strategies to adjust the band structure of g-C_3N_4 are operated at the atomic level (such as elemental doping) and the molecular level (such as copolymerization).

On one hand, elemental doping plays an essential role in tuning the electronic structure of g-C_3N_4. Non-metal doping occurs via substitution of the C or N atoms, which affects the corresponding CB and VB, while metal doping occurs via insertion into the framework of g-C_3N_4. In most cases, a decreased bandgap can be obtained, resulting in extending the light absorption ability. This is quite a flexible strategy that enables the bandgap engineering of g-C_3N_4 by choosing specific doping elements and their amounts, depending on the desired band positions. On the other hand, molecular doping is a unique way for modifying the bandgap of g-C_3N_4 but is usually not available for inorganic semiconductors. Anchoring a very small amount of structure matching organic groups at the edges of g-C_3N_4 nanosheets can significantly affect its bandgap and light-harvesting ability. The doping amount of organic additives can be changed to obtain g-C_3N_4 with the desired bandgap. To illustrate the bandgap engineering of g-C_3N_4 by both elemental doping and molecular doping, the band structures of some typical samples of modified g-C_3N_4 are summarized in **Figure 9** [55].

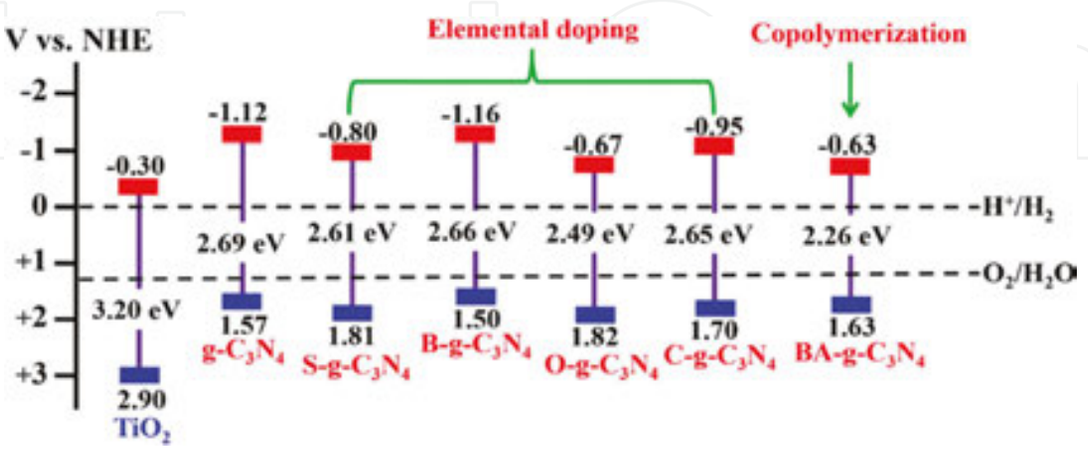


Figure 9. Schematic illustration of the band structures of typical samples of g-C_3N_4 in comparison with TiO_2 (reproduced with permission from [55]).

http://dx.doi.org/10.5772/62889

5.3. g-C_3N_4-based semiconductor composites

To develop effective g-C_3N_4-based nanocomposites with enhanced photocatalytic performance, several main requirements must be considered. Firstly, the composite semiconductor should absorb efficient sunlight. Secondly, the photogenerated charges should be separated effectively and the transfer process should be accelerated. Thirdly, the composite semiconductor must have sufficient redox potential for the desired photochemical reactions. Finally, the composite semiconductor should be stable during the photocatalytic reaction process [56]. Of course, it is difficult to meet all these requirements for a single-material system, while the composite photocatalysts may have the potential to achieve these goals.

So far, a large number of semiconductors have been coupled with g-C_3N_4 to form semiconductor–semiconductor heterojunctions. Among them, two types of heterojunctions have been mainly investigated: traditional type-II heterojunctions and all-solid-state Z-scheme heterojunctions.

A g-C_3N_4-based traditional type-II heterojunction is constructed using g-C_3N_4 and another semiconductor, in which both the CB and VB positions of the g-C_3N_4 are higher or lower than those of another semiconductor. Due to the difference of chemical potential between the two semiconductor units, the band at the contact interface of the heterojunction could bend. This band bending induces to a built-in electric field, resulting in an opposite migration of photogenerated electrons and holes (**Figure 10a**) [57]. For example, g-C_3N_4/In_2O_3 heterojunctions were prepared by in situ growth of In_2O_3 nanocrystals on the surface of g-C_3N_4 via dimethyl sulfoxide (DMSO)-assisted solvothermal method [58]. The traditional type-II heterojunction has been proved to be an efficient method for spatial charge separation. However, the major shortcoming of this heterojunction is the weaker redox ability of the photogenerated electrons and holes originated from the less-negative CB of semiconductor II and the less-positive VB of semiconductor I. Hence, it is difficult to achieve both of the outstanding charge separation efficiency and a strong redox ability for the traditional type-II heterojunction. Fortunately, a new type of all-solid-state Z-scheme heterojunction has been developed recently [59], which could overcome these shortcomings. There are two main types of all-solid-state Z-scheme heterojunctions: semiconductor–semiconductor (S–S) Z-scheme heterojunctions (**Figure 10b**) and semiconductor–conductor–semiconductor (S–C–S) Z-scheme heterojunctions (**Figure 10c**). Such a heterojunction allows for the utilization of semiconductor pairs with narrow bandgap without losing the strong redox ability of the photo-induced electrons and holes. In the S–S Z-scheme heterojunction, the photogenerated electrons from semiconductor II with less-negative CB tend to transfer to semiconductor I with less-positive VB via the contact interface and are further excited to the CB of semiconductor I to participate in the reduction reaction, leaving holes in the VB of semiconductor II to involve into the oxidation reaction. For example, Kumar et al. [60] reported the synthesis of N-doped ZnO/g-C_3N_4 hybrid core–shell nanoplates via a dispersion–evaporation method. By investigating the reactive species of the photocatalytic degradation of rhodamine B in the presence of N-doped ZnO/g-C_3N_4 core–shell structures, a mechanism for S–S Z-scheme heterojunction was proposed. In the case of the S–C–S Z-scheme heterojunction, the conductor material between the two semiconductors serves as an electron mediator to enable the migration of photo-induced electrons from semiconduc-

tor II to semiconductor I. For example, Katsumata et al. [61] obtained a similar S–C–S Z-scheme heterojunction composed of Ag_3PO_4, Ag, and g-C_3N_4 for the efficient photocatalytic decolorization of methyl orange.

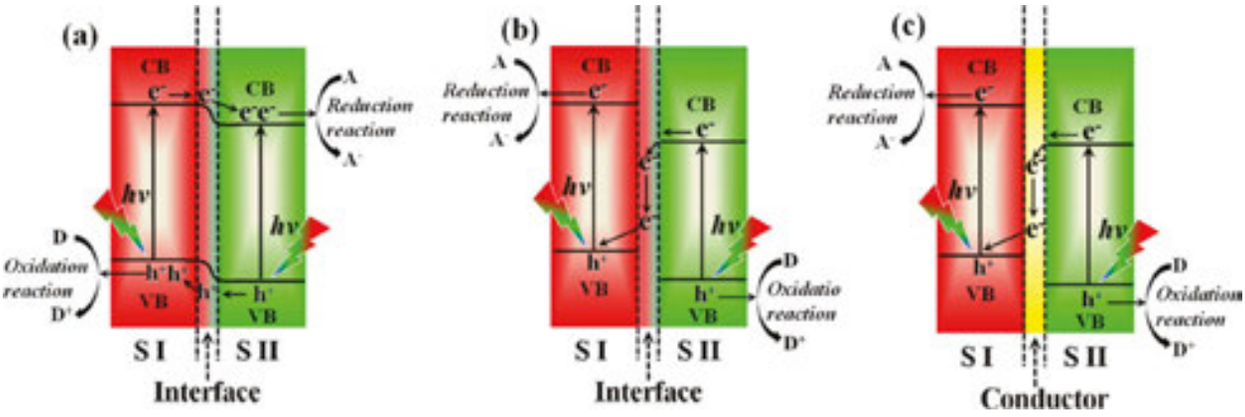


Figure 10. Proposed transfer pathways of photo-induced carriers for different semiconductor heterojunctions: traditional type II heterojunction (a), all solid-state S–S Z-scheme heterojunction (b), all-solid-state S–C–S Z-scheme heterojunction (c). The abbreviations of A, D, S I, and S II denote the electron acceptor, electron donor, semiconductor I, and semiconductor II, respectively (reproduced with permission from [59]).

5.4. Photocatalytic applications of g-C_3N_4

g-C_3N_4 can be used for various photocatalytic applications, such as water splitting, CO_2 reduction, pollutant degradation, organic syntheses, and bacteria disinfection. Remarkable accomplishments have been already achieved in the area of the g-C_3N_4-based photocatalytic hydrogen evolution by dye sensitization, hybridization with carbon materials, and introduction of non-noble-metal co-catalysts. Also, g-C_3N_4/carbon composites and g-C_3N_4-based all-solid-state Z-scheme heterojunctions have been shown to be superior for the photocatalytic degradation of organic pollutants. However, visible-light photocatalytic efficiency of g-C_3N_4 is still relatively low and far from the requirements of practical applications. Therefore, it is required to develop higher performance g-C_3N_4-based photocatalysts in the future.

Acknowledgements

This work is financially supported by the National Natural Science Foundation of China (Grant No. 21403184), National Natural Science Foundation of China (No. 21276220), Natural Science Foundation of the Jiangsu Higher Education Institutions of China (Grant Nos. 14KJB150025, 15KJA430007, and 14KJB430023), China Postdoctoral Science Foundation (No. 2014M561622), Jiangsu Collaborative Innovation Center for Ecological Building Materials and Environmental Protection Equipments (No. GX2015102).

Author details

Pengyu Dong*, Xinguo Xi and Guihua Hou

*Address all correspondence to: dongpy11@gmail.com

Key Laboratory for Advanced Technology in Environmental Protection of Jiangsu Province/ Jiangsu Collaborative Innovation Center for Ecological Building Materials and Environmental Protection Equipments/Yancheng Institute of Technology, Yancheng, Jiangsu Province, China

References

[1] K. Nakata, A. Fujishima. TiO_2 photocatalysis: design and applications. J. Photochem. Photobiol., C, 13 (2012) 169–189.

[2] A. Fujishima, K. Honda. Photolysis-decomposition of water at the surface of an irradiated semiconductor. Nature., 238 (1972) 37–38.

[3] A. Kudo, Y. Miseki. Heterogeneous photocatalyst materials for water splitting. Chem. Soc. Rev., 38 (2009) 253–278.

[4] K. Maeda. Photocatalytic water splitting using semiconductor particles: history and recent developments. J. Photochem. Photobiol., C, 12 (2011) 237–268.

[5] T. Inoue, A. Fujishima, S. Konishi, K. Honda. Photoelectrocatalytic reduction of carbon dioxide in aqueous suspensions of semiconductor powders. Nature., 277 (1979) 637–638.

[6] K. Sunada, T. Watanabe, K. Hashimoto. Bactericidal activity of copper-deposited TiO_2 thin film under weak UV light illumination. Environ. Sci. Technol., 37 (2003) 4785–4789.

[7] S. Yin, Y. Aita, M. Komatsu, J. Wang, Q. Tang, T. Sato. Synthesis of excellent visible-light responsive $TiO_{2-x}N_y$ photocatalyst by a homogeneous precipitation-solvothermal process. J. Mater. Chem., 15 (2005) 674–682.

[8] K. Hashimoto, H. Irie, A. Fujishima. TiO_2 photocatalysis: a historical overview and future prospects. Jpn. J. Appl. Phys., 44 (2005) 8269.

[9] P. Dong, B. Liu, Y. Wang, H. Pei, S. Yin. Enhanced photocatalytic activity of (Mo, C)-codoped anatase TiO_2 nanoparticles for degradation of methyl orange under simulated solar irradiation. J. Mater. Res., 25 (2010) 2392–2400

[10] H. Tong, S. Ouyang, Y. Bi, N. Umezawa, M. Oshikiri, J. Ye. Nano-photocatalytic materials: possibilities and challenges. Adv. Mater., 24 (2012) 229–251.

[11] H. Zheng, J.Z. Ou, M.S. Strano, R.B. Kaner, A. Mitchell, K. Kalantar-zadeh. Nanostructured tungsten oxide—properties, synthesis, and applications. Adv. Funct. Mater., 21 (2011) 2175–2196.

[12] I.M. Szilágyi, B. Fórizs, O. Rosseler, Á. Szegedi, P. Németh, P. Király, G. Tárkányi, B. Vajna, K. Varga-Josepovits, K. László. WO_3 photocatalysts: influence of structure and composition. J. Catal., 294 (2012) 119–127.

[13] S. Gullapalli, R. Vemuri, C. Ramana. Structural transformation induced changes in the optical properties of nanocrystalline tungsten oxide thin films. Appl. Phys. Lett., 96 (2010) 1903.

[14] M. Gillet, K. Aguir, C. Lemire, E. Gillet, K. Schierbaum. The structure and electrical conductivity of vacuum-annealed WO_3 thin films. Thin. Solid. Films., 467 (2004) 239–246.

[15] M. Grätzel. Photoelectrochemical cells. Nature., 414 (2001) 338–344.

[16] H. Zhang, G. Chen, D.W. Bahnemann. Photoelectrocatalytic materials for environmental applications. J. Mater. Chem., 19 (2009) 5089–5121.

[17] D. Monllor-Satoca, L. Borja, A. Rodes, R. Gómez, P. Salvador. Photoelectrochemical behavior of nanostructured WO_3 thin-film electrodes: the oxidation of formic acid. ChemPhysChem., 7 (2006) 2540–2551.

[18] Z.-G. Zhao, M. Miyauchi. Nanoporous-walled tungsten oxide nanotubes as highly active visible-light-driven photocatalysts. Angew. Chem., 120 (2008) 7159–7163.

[19] M. Sadakane, K. Sasaki, H. Kunioku, B. Ohtani, R. Abe, W. Ueda. Preparation of 3-D ordered macroporous tungsten oxides and nano-crystalline particulate tungsten oxides using a colloidal crystal template method, and their structural characterization and application as photocatalysts under visible light irradiation. J. Mater. Chem., 20 (2010) 1811–1818.

[20] R. Abe, H. Takami, N. Murakami, B. Ohtani. Pristine simple oxides as visible light driven photocatalysts: highly efficient decomposition of organic compounds over platinum-loaded tungsten oxide. J. Am. Chem. Soc., 130 (2008) 7780–7781.

[21] M. Miyauchi, Photocatalysis and photoinduced hydrophilicity of WO_3 thin films with underlying Pt nanoparticles. Phys. Chem. Chem. Phys., 10 (2008) 6258–6265.

[22] Z. Yi, J. Ye, N. Kikugawa, T. Kako, S. Ouyang, H. Stuart-Williams, H. Yang, J. Cao, W. Luo, Z. Li. An orthophosphate semiconductor with photooxidation properties under visible-lightirradiation. Nat. Mater., 9 (2010) 559–564.

[23] H. Wang, Y. Bai, J. Yang, X. Lang, J. Li, L. Guo. A facile way to rejuvenate Ag_3PO_4 as a recyclable highly efficient photocatalyst. Chem. A Eur. J., 18 (2012) 5524–5529.

[24] Y. Bi, S. Ouyang, J. Cao, J. Ye. Facile synthesis of rhombic dodecahedral AgX/Ag_3PO_4 (X = Cl, Br, I) heterocrystals with enhanced photocatalytic properties and stabilities. Phys. Chem. Chem. Phys., 13 (2011) 10071–10075.

[25] Y. Bi, S. Ouyang, N. Umezawa, J. Cao, J. Ye. Facet effect of single-crystalline Ag_3PO_4 sub-microcrystals on photocatalytic properties. J. Am. Chem. Soc., 133 (2011) 6490–6492.

[26] J.-K. Liu, C.-X. Luo, J.-D. Wang, X.-H. Yang, X.-H. Zhong. Controlled synthesis of silver phosphate crystals with high photocatalytic activity and bacteriostatic activity. CrystEngComm., 14 (2012) 8714–8721.

[27] H. Wang, L. He, L. Wang, P. Hu, L. Guo, X. Han, J. Li. Facile synthesis of Ag_3PO_4 tetrapod microcrystals with an increased percentage of exposed {110} facets and highly efficient photocatalytic properties. CrystEngComm., 14 (2012) 8342–8344.

[28] W. Jun, F. Teng, M. Chen. Facile synthesis of novel Ag_3PO_4 tetrapods and the {110} facets-dominated photocatalytic activity. CrystEngComm., 15 (2013) 39–42.

[29] Q. Liang, W. Ma, Y. Shi, Z. Li, X. Yang. Hierarchical Ag_3PO_4 porous microcubes with enhanced photocatalytic properties synthesized with the assistance of trisodium citrate. CrystEngComm., 14 (2012) 2966–2973.

[30] P. Dong, Y. Wang, H. Li, H. Li, X. Ma, L. Han. Shape-controllable synthesis and morphology-dependent photocatalytic properties of Ag_3PO_4 crystals. J. Mater. Chem. A, 1 (2013) 4651–4656.

[31] G.-F. Huang, Z.-L. Ma, W.-Q. Huang, Y. Tian, C. Jiao, Z.-M. Yang, Z. Wan, A. Pan. Ag_3PO_4 semiconductor photocatalyst: possibilities and challenges. J. Nanomater., 2013 (2013) 1.

[32] N. Umezawa, O. Shuxin, J. Ye. Theoretical study of high photocatalytic performance of Ag_3PO_4. Phys. Rev. B, 83 (2011) 035202.

[33] X. Ma, B. Lu, D. Li, R. Shi, C. Pan, Y. Zhu. Origin of photocatalytic activation of silver orthophosphate from first-principles. J. Phys. Chem. C, 115 (2011) 4680–4687.

[34] W. Yao, B. Zhang, C. Huang, C. Ma, X. Song, Q. Xu. Synthesis and characterization of high efficiency and stable Ag_3PO_4/TiO_2 visible light photocatalyst for the degradation of methylene blue and rhodamine B solutions. J. Mater. Chem., 22 (2012) 4050–4055.

[35] Y. Liu, L. Fang, H. Lu, Y. Li, C. Hu, H. Yu. One-pot pyridine-assisted synthesis of visible-light-driven photocatalyst Ag/Ag_3PO_4. Appl. Catal. B, 115–116 (2012) 245–252.

[36] P. Dong, Y. Wang, B. Cao, S. Xin, L. Guo, J. Zhang, F. Li. Ag_3PO_4/reduced graphite oxide sheets nanocomposites with highly enhanced visible light photocatalytic activity and stability. Appl. Catal. B, 132–133 (2013) 45–53.

[37] P. Dong, E. Cui, G. Hou, R. Guan, Q. Zhang. Synthesis and photocatalytic activity of $Ag_3PO_4/TiOF_2$ composites with enhanced stability. Mater. Lett., 143 (2015) 20–23.

[38] J.H. Kim, J.S. Lee. $BiVO_4$-based heterostructured photocatalysts for solar water splitting: a review. Energy. Environ. Focus, 3 (2014) 339–353.

[39] A. Kudo, K. Omori, H. Kato. A novel aqueous process for preparation of crystal form-controlled and highly crystalline $BiVO_4$ powder from layered vanadates at room temperature and its photocatalytic and photophysical properties. J. Am. Chem. Soc., 121 (1999) 11459–11467.

[40] S. Tokunaga, H. Kato, A. Kudo. Selective preparation of monoclinic and tetragonal $BiVO_4$ with scheelite structure and their photocatalytic properties. Chem. Mater., 13 (2001) 4624–4628.

[41] L. Zhang, D. Chen, X. Jiao. Monoclinic structured $BiVO_4$ nanosheets: hydrothermal preparation, formation mechanism, and coloristic and photocatalytic properties. J. Phys. Chem. B, 110 (2006) 2668–2673.

[42] L. Zhou, W. Wang, L. Zhang, H. Xu, W. Zhu. Single-crystalline $BiVO_4$ microtubes with square cross-sections: microstructure, growth mechanism, and photocatalytic property. J. Phys. Chem. C, 111 (2007) 13659–13664.

[43] G. Li, D. Zhang, J.C. Yu. Ordered mesoporous $BiVO_4$ through nanocasting: a superior visible light-driven photocatalyst. Chem. Mater., 20 (2008) 3983–3992.

[44] R. Li, F. Zhang, D. Wang, J. Yang, M. Li, J. Zhu, X. Zhou, H. Han, C. Li. Spatial separation of photogenerated electrons and holes among {010} and {110} crystal facets of $BiVO_4$. Nat. Commun., 4 (2013) 1432.

[45] B. Liu, Y. Fang, Z. Li, S. Xu. Visible-light nanostructured photocatalysts—a review. J. Nanosci. Nanotechnol., 15 (2015) 889–920.

[46] S.J. Hong, S. Lee, J.S. Jang, J.S. Lee. Heterojunction $BiVO_4/WO_3$ electrodes for enhanced photoactivity of water oxidation. Energy Environ. Sci., 4 (2011) 1781–1787.

[47] J. Su, L. Guo, N. Bao, C.A. Grimes. Nanostructured $WO_3/BiVO_4$ heterojunction films for efficient photoelectrochemical water splitting. Nano Lett., 11 (2011) 1928–1933.

[48] R. Saito, Y. Miseki, K. Sayama. Highly efficient photoelectrochemical water splitting using a thin film photoanode of $BiVO_4/SnO_2/WO_3$ multi-composite in a carbonate electrolyte. Chem. Commun., 48 (2012) 3833–3835.

[49] F.F. Abdi, T.J. Savenije, M.M. May, B. Dam, R. van de Krol. The origin of slow carrier transport in $BiVO_4$ thin film photoanodes: a time-resolved microwave conductivity Study. J. Phys. Chem. Lett., 4 (2013) 2752–2757.

[50] P. Chatchai, Y. Murakami, S.-Y. Kishioka, A. Nosaka, Y. Nosaka. $FTO/SnO_2/BiVO_4$ composite photoelectrode for water oxidation under visible light irradiation. Electrochem. Solid State Lett., 11 (2008) H160–H163.

[51] X. Wang, K. Maeda, A. Thomas, K. Takanabe, G. Xin, J.M. Carlsson, K. Domen, M. Antonietti. A metal-free polymeric photocatalyst for hydrogen production from water under visible light. Nat. Mater., 8 (2009) 76–80.

[52] A. Thomas, A. Fischer, F. Goettmann, M. Antonietti, J.-O. Müller, R. Schlögl, J.M. Carlsson. Graphitic carbon nitride materials: variation of structure and morphology and their use as metal-free catalysts. J. Mater. Chem., 18 (2008) 4893–4908.

[53] W. Shen, L. Ren, H. Zhou, S. Zhang, W. Fan. Facile one-pot synthesis of bimodal mesoporous carbon nitride and its function as a lipase immobilization support. J. Mater. Chem., 21 (2011) 3890–3894.

[54] Y. Cui, Z. Ding, X. Fu, X. Wang. Construction of conjugated carbon nitride nanoarchitectures in solution at low temperatures for photoredox catalysis. Angew. Chem. Int. Ed., 51 (2012) 11814–11818.

[55] S. Cao, J. Low, J. Yu, M. Jaroniec. Polymeric photocatalysts based on graphitic carbon nitride. Adv. Mater., 27 (2015) 2150–2176.

[56] Z. Zhao, Y. Sun, F. Dong. Graphitic carbon nitride based nanocomposites: a review. Nanoscale, 7 (2015) 15–37.

[57] Y. Wang, Q. Wang, X. Zhan, F. Wang, M. Safdar, J. He. Visible light driven type II heterostructures and their enhanced photocatalysis properties: a review. Nanoscale, 5 (2013) 8326–8339.

[58] S.-W. Cao, X.-F. Liu, Y.-P. Yuan, Z.-Y. Zhang, Y.-S. Liao, J. Fang, S.C.J. Loo, T.C. Sum, C. Xue. Solar-to-fuels conversion over In_2O_3/gC_3N_4 hybrid photocatalysts. Appl. Catal. B, 147 (2014) 940–946.

[59] P. Zhou, J. Yu, M. Jaroniec. All-solid-state Z-scheme photocatalytic systems. Adv. Mater., 26 (2014) 4920–4935.

[60] S. Kumar, A. Baruah, S. Tonda, B. Kumar, V. Shanker, B. Sreedhar. Cost-effective and eco-friendly synthesis of novel and stable N-doped ZnO/gC_3N_4 core–shell nanoplates with excellent visible-light responsive photocatalysis. Nanoscale, 6 (2014) 4830–4842.

[61] H. Katsumata, T. Sakai, T. Suzuki, S. Kaneco. Highly efficient photocatalytic activity of $g\text{-}C_3N_4/Ag_3PO_4$ hybrid photocatalysts through Z-scheme photocatalytic mechanism under visible light. Ind. Eng. Chem. Res., 53 (2014) 8018–8025.

IntechOpen

IntechOpen